AGU PUBLICATIONS

Geochemistry, Geophysics, Geosystems

RESEARCH ARTICLE
10.1002/2016GC006344

Key Points:
- We have identified a lagged marine diagenetic record that correlates with changes in Asian monsoon fluctuations
- The correlation was determined by identifying offsets between positions of fossil diagenetic fronts and variations in organic carbon burial
- Relict titanomagnetite inclusions dominate the diagenetically altered sediment intervals and are protected against sulfidic dissolution

Supporting Information:
- Supporting Information S1

Correspondence to:
L. Chang,
liao.chang@pku.edu.cn

Citation:
Chang, L., et al. (2016), Asian monsoon modulation of nonsteady state diagenesis in hemipelagic marine sediments offshore of Japan, *Geochem. Geophys. Geosyst.*, *17*, doi:10.1002/2016GC006344.

Received 8 MAR 2016
Accepted 12 OCT 2016
Accepted article online 17 OCT 2016

Asian monsoon modulation of nonsteady state diagenesis in hemipelagic marine sediments offshore of Japan

Liao Chang[1,2], Clara T. Bolton[3], Mark J. Dekkers[4], Akira Hayashida[5], David Heslop[2], Wout Krijgsman[4], Kazuto Kodama[6], Greig A. Paterson[7], Andrew P. Roberts[2], Eelco J. Rohling[2], Yuhji Yamamoto[6], and Xiang Zhao[2]

[1]School of Earth and Space Sciences, Peking University, Beijing, People's Republic of China, [2]Research School of Earth Sciences, Australian National University, Canberra, Australian Capital Territory, Australia, [3]Université Aix-Marseille, CNRS, IRD, CEREGE UM34, Aix en Provence, France, [4]Paleomagnetic Laboratory 'Fort Hoofddijk', Department of Earth Sciences, Utrecht University, Utrecht, Netherlands, [5]Department of Environmental Systems Science, Doshisha University, Kyotanabe, Japan, [6]Center for Advanced Marine Core Research, Kochi University, Kochi, Japan, [7]Key Laboratory of Earth and Planetary Physics, Institute of Geology and Geophysics, Chinese Academy of Sciences, Beijing, People's Republic of China

Abstract We have identified millennial-scale variations in magnetic mineral diagenesis from Pacific Ocean sediments offshore of Japan that we correlate with changes in organic carbon burial that were likely driven by Asian monsoon fluctuations. The correlation was determined by identifying offsets between the positions of fossil diagenetic fronts and climatically induced variations in organic carbon burial inferred from magnetic and geochemical analyses. Episodes of intense monsoon activity and attendant sediment magnetic mineral diagenesis also appear to correlate with Heinrich events, which supports the existence of climatic telecommunications between Asia and the North Atlantic region. Several lines of evidence support our conclusions: (1) fluctuations in down-core magnetic properties and diagenetic pyrite precipitation are approximately coeval; (2) localized stratigraphic intervals with relatively stronger magnetic mineral dissolution are linked to enhanced sedimentary organic carbon contents that gave rise to nonsteady state diagenesis; (3) down-core variations in elemental S content provide a proxy for nonsteady state diagenesis that correlate with key records of Asian monsoon variations; and (4) relict titanomagnetite that is preserved as inclusions within silicate particles, rather than secondary authigenic phases (e.g., greigite), dominates the strongly diagenetically altered sediment intervals and are protected against sulfidic dissolution. We suggest that such millennial-scale environmental modulation of nonsteady state diagenesis (that creates a temporal diagenetic filter and relict magnetic mineral signatures) is likely to be common in organic-rich hemipelagic sedimentary settings with rapidly varying depositional conditions. Our work also demonstrates the usefulness of magnetic mineral inclusions for recording important environmental magnetic signals.

1. Introduction

Paleomagnetism provides a primary dating tool for sedimentary sequences [*Opdyke and Channell*, 1996] and has made fundamental contributions to understanding geomagnetic field behavior and geodynamo processes [*Valet et al.*, 2005]. Environmental magnetic analysis of sedimentary sequences also provides insights into the formation, transportation, and postdepositional alteration of magnetic minerals within sediments and has been widely used to study large-scale climatic and environmental processes [*Thompson and Oldfield*, 1986; *Liu et al.*, 2012; *Roberts*, 2015]. Use of sedimentary magnetic properties depends crucially on developing a thorough understanding of magnetic minerals within sediments (i.e., magnetic mineralogy and grain size). This also requires understanding of the interactions of magnetic mineral grains with physical and chemical processes in sedimentary depositional environments [*Karlin*, 1990a, 1990b].

Hemipelagic sediments along continental margins are often targeted for high-resolution paleoenvironmental and paleomagnetic studies because of their rapid terrigenous and biogenic sedimentation and geographically widespread occurrence. Hemipelagic sediments are often rich in organic carbon (OC, either from fluvially derived terrestrial sources or marine productivity), the gradual degradation and oxidation of which in different biogeochemical zones, often mediated by microorganisms, can strongly affect sedimentary records [*Karlin and Levi*, 1983, 1985; *Karlin*, 1990a, 1990b; *Roberts and Turner*, 1993; *Tarduno and Wilkison*, 1996; *Emiroğlu et al.*, 2004; *Garming et al.*, 2005; *Dillon and Bleil*, 2006; *Rowan et al.*, 2009; *Roberts*, 2015]. The reductive diagenesis

that typically occurs in sulfidic environments involves oxidation of organic matter mediated by dissimilatory sulfate reduction or anaerobic oxidation of methane (CH_4) that releases H_2S to react with detrital iron-bearing minerals, which gives rise to their dissolution and widespread pyrite precipitation [e.g., *Schulz and Zabel*, 2006]. Microbially mediated diagenesis in marine environments plays an important role in global cycles of carbon, iron, and sulfur [e.g., *Schulz and Zabel*, 2006]. Magnetic mineral diagenesis—even during earliest burial—is recognized to be a fundamentally important process, which makes it important to be able to assess the extent of diagenetic modification in sedimentary magnetic studies [*Roberts*, 2015].

The effects of nonsteady state diagenesis on magnetic records [e.g., *Tarduno*, 1994; *van Santvoort et al*., 1997; *Roberts et al*., 1999; *Larrasoaña et al*., 2003] have been less well studied than more pervasive steady state scenarios because of the complex sum of competing biogeochemical reactions due to variable supply, burial, and degradation of OC and electron acceptor availability. *Karlin* [1990b] described magnetic peaks at depth and attributed them to nonsteady state magnetic mineral diagenesis. *Tarduno* [1994] observed hysteresis parameter variations that are linked to oxygen isotope variations in the western equatorial Pacific Ocean and argued for nonsteady state diagenesis linked to glacial-interglacial OC supply. *Sahota et al*. [1995] described oxidative burndown through turbidities as an end-member of nonsteady state conditions. *Passier et al*. [2001] and *Passier and Dekkers* [2002] studied the effects of nonsteady state diagenesis on the magnetic properties of Mediterranean sapropels with large OC supply changes, while *Larrasoaña et al*. [2003] documented long-term magnetic property variations that were driven by climatically controlled, nonsteady state OC flux in eastern Mediterranean sediments. Several other studies also demonstrate the complexities associated with nonsteady state magnetic mineral diagenesis in sedimentary records [e.g., *Riedinger et al*., 2005; *Blanchet et al*., 2009; *Itambi et al*., 2010; *Abrajevitch and Kodama*, 2011; *Kawamura et al*., 2012; *Bouilloux et al*., 2013; *Roberts*, 2015].

In this study, we carried out integrated magnetic and geochemical analyses, supported by electron microscope observations, on a deep-sea sediment core from offshore of Japan, western Pacific Ocean, to investigate the effects of sedimentary diagenetic alteration, and to study paleoenvironmental changes in East Asia over the last glacial cycle. Sediments in the studied core [*Oba et al*., 2006] were deposited rapidly (~30 cm/kyr) in a highly dynamic sedimentary setting and are rich in organic matter (average of 1.2 wt % total OC (TOC)), which offers an excellent opportunity to study potential millennial-scale paleoenvironmental changes and their effects on sedimentary diagenesis under shifting depositional conditions.

2. Core MD01-2421 and Sediment Materials

Piston core MD01-2421 was recovered ~100 km offshore of central Japan (36°01.4′N; 141°46.8′E; 2224 m water depth; core length of 45.82 m). It was recovered by the French R/V *Marion Dufresne* during IMAGES (International Marine Global Change Study) cruise VII-WEPAMA (Western Pacific Margin) Leg 2 in 2001 [*Oba et al*., 2006]. The studied site is from the Northwest Pacific Ocean, where the cold Oyashio and warm Kuroshio currents interact. It, therefore, lies within a sensitive region for monitoring the migration of western boundary currents in the North Pacific Ocean in response to past climate change (Figure 1) [*Oba et al*., 2006]. The core site is located on relatively flat seafloor on a convex submarine plateau on the continental slope. Although the site is on a tectonically active margin with frequent earthquake events, *Oba et al*. [2006] documented a lack of distinct turbidite layers at the core site due to its bathymetric setting.

The sediment in core MD01-2421 is a homogenous olive-gray silty clay with abundant calcareous and siliceous microfossils. TOC varies between 0.5 and 2.1 wt % [*Ueshima et al*., 2006], which indicates a relatively high input and preservation of organic matter. The age model for the core is well established and is based on a combination of oxygen isotope stratigraphy of the benthic foraminifera *Uvigerina* and *Bulimina aculeata*, ^{14}C ages of 12 samples of mixed planktonic foraminifera (*Neogloboquadrina dutertrei* and *Globorotalia inflata*; 0.31–43.33 ka), and by the Aira-Tn ash layer at 28.59 ka [*Oba et al*., 2006, Table 2]. The sediments were deposited continuously with an age of 144 ka in marine isotope stage (MIS) 6 at the bottom of the core. Details of the age model of the studied core can be found in *Oba et al*. [2006].

3. Methods

Continuous X-ray fluorescence (XRF) and magnetic measurements, including volume normalized magnetic susceptibility (κ), anhysteretic remanent magnetization (ARM), and isothermal remanent magnetization

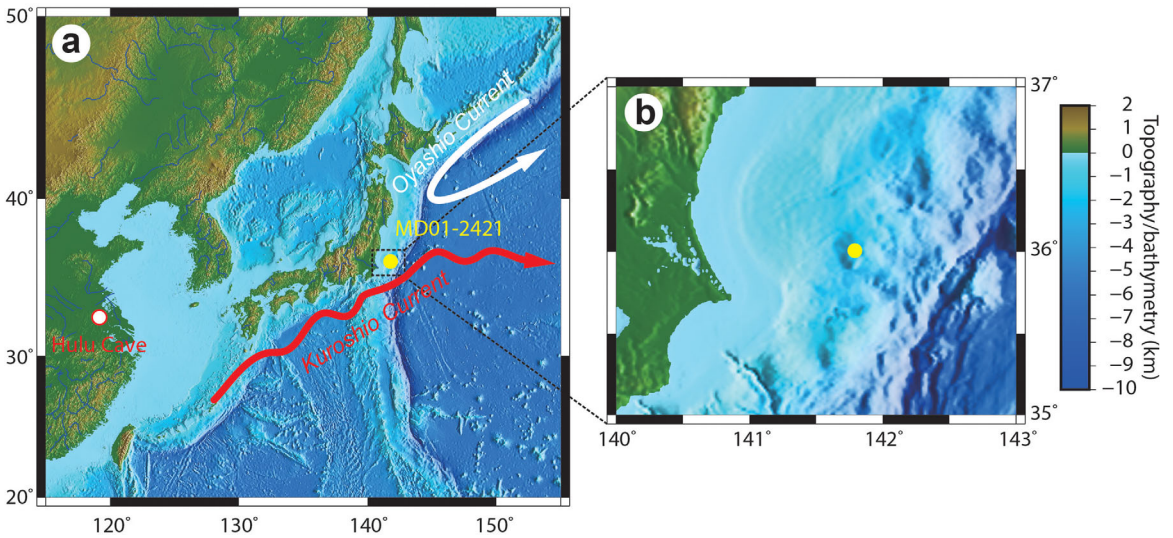

Figure 1. (a) Location of the studied sediment core MD01-2421 (yellow solid circle), off the east coast of Japan. (b) An enlarged view of the dashed area in Figure 1a that surrounds the core site. The Kuroshio and Oyashio currents are indicated in Figure 1a. The location of Hulu Cave is marked by a red circle in Figure 1a.

(IRM) measurements, were made on u-channel samples [*Weeks et al.*, 1993]. XRF analysis was performed on u-channels to measure concentration variations of major elements, using a JSX-3600 CAZ (TATSCAN-F2) XRF core scanner at the Kochi Core Center (KCC), Kochi University, Japan. Discrete samples were collected from the top of the core to a depth of 34 m at sampling intervals of 10–60 cm. Discrete samples were freeze-dried and were subjected to hysteresis, IRM acquisition, and backfield remanent magnetization (∼100 samples), first-order reversal curve (FORC; ∼40 samples), thermomagnetic (∼30 samples), and low-temperature magnetic (∼10 samples) measurements. Hysteresis loops, IRM acquisition, backfield demagnetization, and FORC measurements were carried out at the KCC and at Utrecht University, Netherlands, using a Princeton Measurements Corporation MicroMag alternating gradient magnetometer (AGM) (Model 2900; noise level 2×10^{-9} Am^2). Hysteresis loops were measured between −1 and +1 T with a field step of 5 mT and an averaging time of 150 ms. The saturation magnetization (M_s), saturation remanent magnetization (M_{rs}), and coercivity (B_c) were determined from hysteresis loops after paramagnetic slope correction. FORC diagrams [*Pike et al.*, 1999; *Roberts et al.*, 2000] were obtained with maximum applied fields of 1 T, field increments up to 0.6 mT and averaging times of 150–250 ms. FORC diagrams were calculated using the FORCme package of *Heslop and Roberts* [2012]. IRM acquisition curves were obtained by measuring 100–150 field steps up to a maximum applied field of 1 T. The coercivity of remanence (B_{cr}) was determined from backfield demagnetization curves.

Thermomagnetic measurements in air were made with a modified horizontal translation-type Curie balance with a sensitivity of $\sim 5 \times 10^{-9}$ Am^2 at Utrecht University [*Mullender et al.*, 1993]. For selected samples, multiple heating and cooling cycles between room temperature, and 200, 300, 350, 450, 620, and 700°C were performed at a heating/cooling rate of 6°C/min. Depending on sample magnetizations, ∼10–100 mg of sediment was used. Low-temperature magnetic properties were measured with a Quantum Design Magnetic Property Measurement System (MPMS; model XL7) at the Australian National University (ANU). For zero-field-cooled (ZFC) and field-cooled (FC) curves, samples were cooled to 10 K in either zero field or a 5 T field. At 10 K, a 5 T field was applied and was then switched off to impart a low-temperature saturation IRM (SIRM); the magnet was then reset (the residual field after a magnet reset is ∼200–300 μT), and SIRM was measured during zero-field warming. For low-temperature cycling (LTC), a room temperature SIRM was cycled between room temperature and 10 K in zero field.

Magnetic mineral separation was performed following the procedure of *Chang et al.* [2012]. Observations of magnetic extracts, using a scanning electron microscope (SEM) and a transmission electron microscope (TEM), were carried out at the Centre for Advanced Microscopy, ANU. SEM observations were made using a Carl Zeiss UltraPlus analytical field emission SEM. High-resolution SEM images were acquired on uncoated samples at 2 kV. Backscattered electron images, secondary electron images, and energy-dispersive spectra

(EDS) were acquired at 15 kV on carbon-coated samples. An INCA ENERGY 450 energy-dispersive X-ray spectroscopy (EDXS) system was used. TEM observations were made with a Philips CM300 TEM operated at 300 kV with an EDAS Phoenix retractable X-ray detector.

4. Results

4.1. Down-Core Magnetic and XRF Profiles

Concentration-dependent magnetic parameters undergo large down-core fluctuations with numerous spikes, including magnetic susceptibility κ, ARM, and IRM data from u-channels (supporting information Figure S1) and hysteresis parameters measured on discrete samples (Figures 2a–2d). Some magnetic peaks in u-channel data are associated with volcanic ash layers. To avoid the strong magnetic spikes associated with tuff layers in the u-channel data, we use hysteresis profiles measured on discrete samples for our interpretation. We intentionally did not sample tuff layers when collecting discrete samples for magnetic analysis. A negative correlation exists between magnetic concentration-dependent parameters (i.e., M_s) and magnetic grain size-dependent parameters (i.e., B_c, B_{cr}, and M_{rs}/M_s) (gray bars in Figures 2a–2d). Elemental S variations (Figure 2e) and TOC (Figure 2f) variations are plotted together with down-core hysteresis parameters. Variations in other elements and their ratios are presented in supporting information Figure S2. Intervals with high magnetic mineral concentration (Figure 2a) and lower B_c values (Figure 2b) correspond to low S and TOC values (Figures 2e and 2f), and *vice versa*. Among these correlations, a similar down-core pattern of B_c (Figure 2b) and S (Figure 2e) is notable. The broad correlations between magnetic and geochemical parameters (Figure 2) indicate interactions between magnetic minerals and geochemical processes.

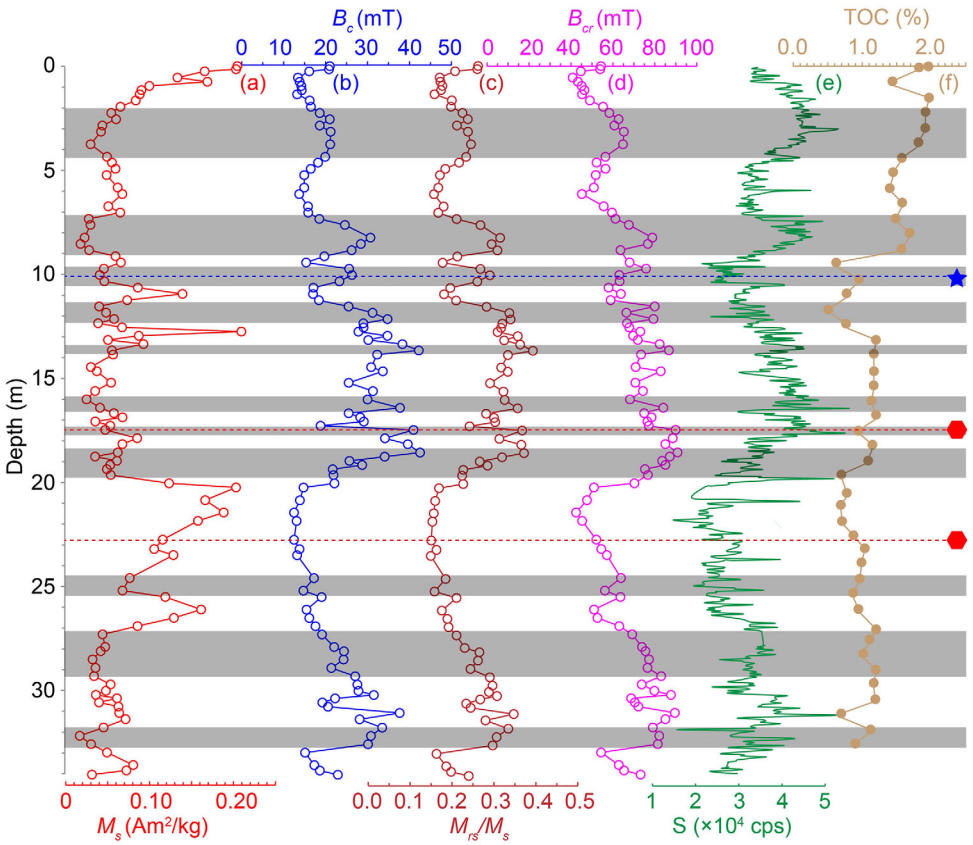

Figure 2. Down-core variations in (a–d) magnetic hysteresis parameters, (e) elemental S abundance, and (f) TOC content for core MD01-2421. Magnetic and geochemical parameters are broadly correlated: high M_s values correlate negatively with grain size sensitive parameters (i.e., low B_c, B_{cr}, and M_{rs}/M_s values), and also with low elemental S content. B_c, B_{cr}, M_{rs}/M_s, and XRF S content have similar down-core variations, except that the S data were measured at higher resolution. Gray bars mark intervals with weaker magnetizations and harder magnetic minerals. The red hexagons and blue star indicate the stratigraphic positions of representative samples for more detailed rock magnetic results (Figure 4) and electron microscope observations (Figure 6), respectively.

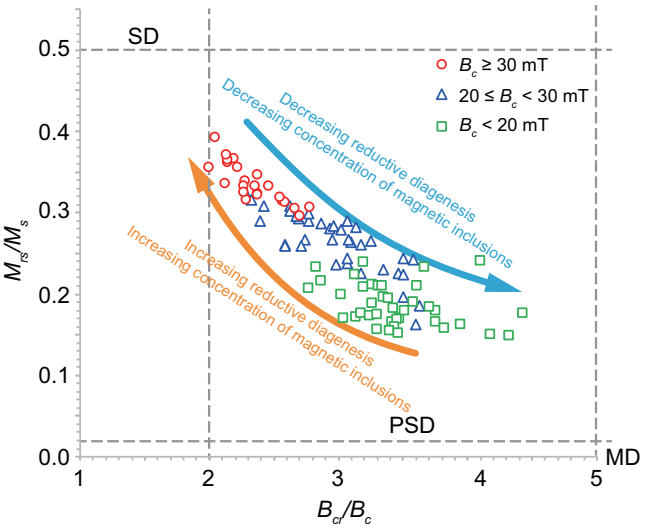

Figure 3. Magnetic hysteresis parameters on a plot of M_{rs}/M_s versus B_{cr}/B_c [*Day et al.*, 1977] for measured samples from core MD01-2421. Areas expected for single domain (SD), pseudo-single-domain (PSD), and multidomain (MD) grains are indicated with dashed lines. Red circles, blue triangles, and green squares indicate samples with $B_c \geq 30$ mT, 20 mT $\leq B_c < 30$ mT, and $B_c < 20$ mT, respectively. Arrows indicate the data trend: with increasing strength of reductive diagenesis, magnetic mineral inclusions become more important, and the data move toward the SD region, and *vice versa*. Details can be found in the discussion section 5.1.

4.2. Magnetic Properties

The measured magnetic properties vary between two major groups throughout the studied core: one is magnetically softer and one is magnetically harder based on coercivity values. Hysteresis ratios for different groups of samples are plotted following *Day et al.* [1977] (Figure 3). Relatively coarse-grained samples have hysteresis parameters with typically lower B_c (i.e., <20 mT) and M_{rs}/M_s values (i.e., <0.24) (Figure 3a). Fine-grained samples have larger B_c (i.e., >30 mT) and M_{rs}/M_s values (i.e., >0.30) (Figure 3b). There is no distinct boundary for B_c values between the hard and soft samples, and there are overlaps in magnetic properties among samples, particularly for those with intermediate B_c values. In Figure 4, we present magnetic properties for two extreme samples ("MD01-2421-12-100" and "MD01-2421-16-30" from depths of 17.48 and 22.74 m, respectively; indicated by red hexagons in Figure 2). Magnetic analyses for a large sample set (data not shown) throughout the core indicate that their magnetic properties fall between those of these two representative samples.

FORC diagrams for coarse-grained samples have characteristic pseudo-single-domain (PSD)/multidomain (MD) properties with divergent distributions at low coercivities (Figure 4c) [e.g., *Roberts et al.*, 2000, 2014; *Pike et al.*, 2001; *Muxworthy and Dunlop*, 2002]. Fine-grained samples have dominantly concentric single-domain (SD)-like FORC distributions [*Roberts et al.*, 2000, 2014], with broad coercivity distributions (up to >300 mT), and relatively small vertical spread (Figure 4d). FORC diagrams for some samples contain evidence of two components: one with a divergent distribution at low fields and one with a SD distribution, which indicate a mixture of fine-grained and coarse-grained magnetic minerals.

IRM component analysis [*Kruiver et al.*, 2001] indicates that most samples can be fitted with one or two major IRM components (Figures 4e and 4f). For the coarse-grained sample, the major IRM component has a median field of 66 mT with a dispersion parameter (DP) value of 0.37 (Figure 4e; magenta line). This component contributes 94% of the IRM. The fine-grained sample also has one major IRM component that contributes 82% to the IRM. This major component has a smaller DP value (0.29; Figure 4f, magenta line) and a higher median field (118 mT). All measured samples have relatively large DP values (mostly >0.33).

Thermomagnetic results for a coarse-grained sample (Figure 4g) indicate a major magnetization loss close to ~580°C, which is the Curie temperature (T_c) of magnetite (Fe_3O_4). The inflection of the heating curve between 300 and 400°C probably indicates the onset of thermal alteration of pyrite [*Passier et al.*, 2001]. The cooling curve has a weaker magnetization than the heating curve, which appears to be due to thermal alteration of magnetite to hematite (α-Fe_2O_3). For a fine-grained sample, the heating curve undergoes a pronounced magnetization drop below 300°C. Multiple heating and cooling measurements indicate that this magnetization drop is nearly reversible (Figure 4h). Extrapolation of this magnetization drop indicates a Curie point below 400°C. The magnetic mineral responsible for this signal cannot be stoichiometric magnetite but is more likely to be titanomagnetite ($Fe_{3-x}Ti_xO_4$, $0 \leq x < 1$). Some samples undergo a small magnetization increase from the heating and cooling cycles below 350°C (e.g., Figure 4h), which may be associated with titanomaghemite inversion during heating [e.g., *Doubrovine and Tarduno*, 2006]. However, this signature is mostly absent or subtle among the studied samples. Many samples also undergo a magnetization increase starting at ~400°C, with peaks mostly between ~440 and 510°C. These peaks probably indicate

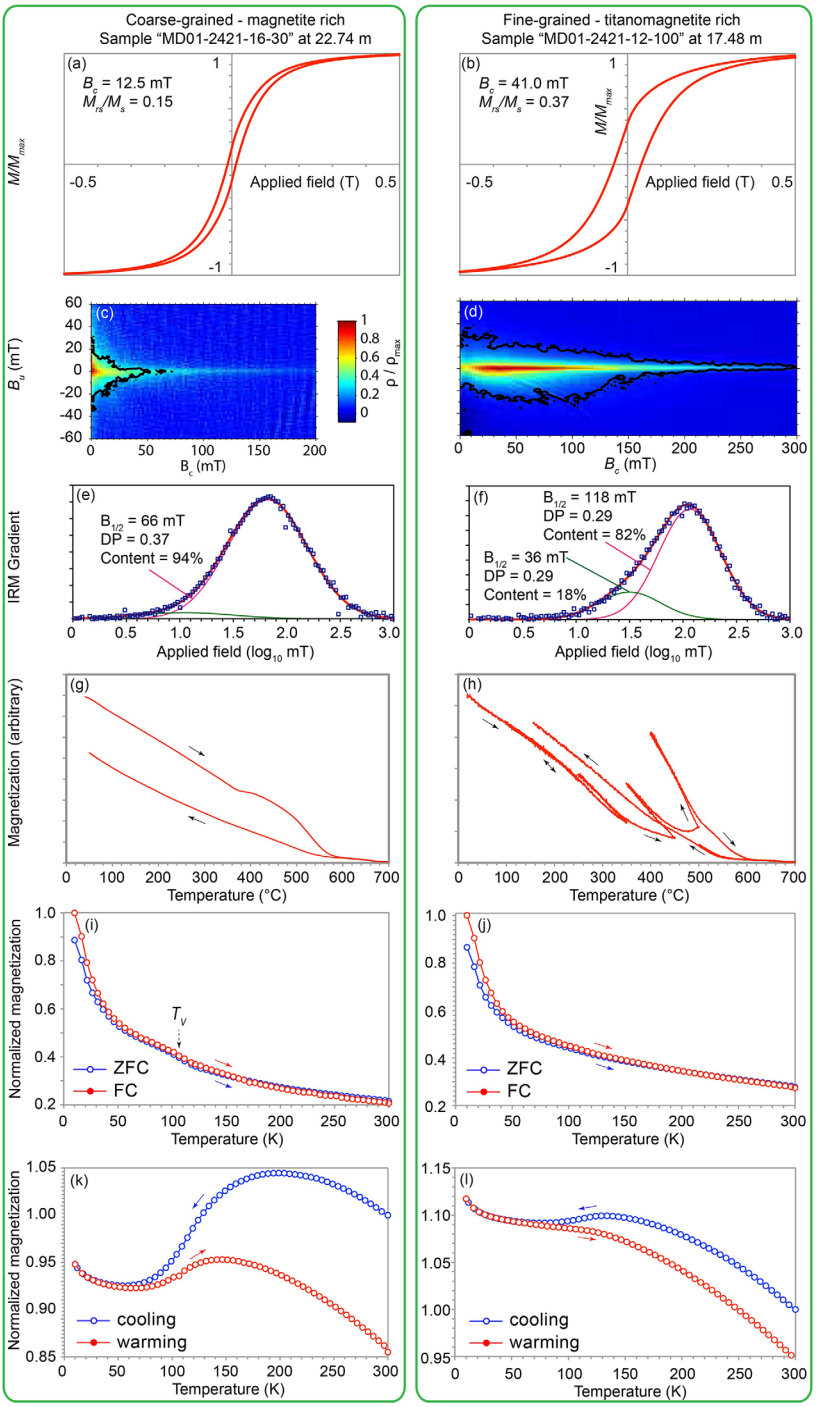

Figure 4. Comparison of magnetic results for two typical sediment samples: (a, c, e, g, i, k) a representative coarse-grained sample ("MD01-2421-16-30," from a depth of 22.74 m), and (b, d, f, h, j, l) a representative fine-grained sample ("MD01-2421-12-100," from a depth of 17.48 m). Many samples were subjected to magnetic measurements; only results for two typical samples are presented here. (a, b) Hysteresis loops, (c, d) FORC diagrams, (e, f) IRM coercivity decomposition analysis, (g, h) thermomagnetic curves, (i, j) low-temperature warming of SIRM curves, and (k, l) LTC curves for a room temperature SIRM. Hysteresis loops (Figures 4a and 4b) are normalized to M_s values (at 1 T) after paramagnetic slope correction. Hysteresis parameters (B_c and M_{rs}/M_s) are indicated. In Figures 4c and 4d, thick black contour lines indicate the regions of the FORC distribution that are significant at the 0.05 level. In Figures 4e and 4f, squares indicate measured IRM data. Thick red lines are the fitted total coercivity spectra. The other lines (magenta and green) represent different fitted components. Fitted parameters for major components are indicated. Thermomagnetic runs (Figures 4g and 4h) were measured in air during heating and cooling cycles (arrows). In Figures 4i and 4j, SIRM warming curves are normalized to the magnetization at 10 K for the FC curves. The vertical arrow in Figure 4i indicates a feint T_v. In Figures 4k and 4l, LTC curves are normalized to the initial SIRM at room temperature.

neoformation of magnetite due to oxidation of sedimentary pyrite during heating (including euhedral and framboidal microtextures) [*Passier et al*., 2001]. Thermomagnetic analysis of selected samples from throughout the studied core indicates that coarse-grained samples have T_c close to 580°C with only subtle pyrite oxidation peaks (supporting information Figure S3a), while lower T_c and large pyrite oxidation peaks are common for fine-grained samples (supporting information Figure S3c). This interpretation is confirmed by measuring samples across the magnetic and elemental S peaks (e.g., supporting information Figure S3 and data not shown).

Low-temperature ZFC/FC SIRM warming curves for the coarse-grained sample have a hint of a Verwey transition temperature (T_v) at around 110 K (Figure 4i), which confirms the presence of magnetite. In contrast, little evidence exists for a T_v in ZFC/FC SIRM warming curves for fine-grained samples (Figure 4j). LTC curves for coarse-grained samples have pronounced humps (Figure 4k), while fine-grained samples have a smaller divergence between the cooling and warming branch of LTC curves (Figure 4l). Low-temperature magnetic results consistently indicate that the studied fine-grained samples contain much less magnetite compared to coarse-grained samples.

4.3. IRM End-Member Modeling

We use IRM end-member (EM) modeling analysis [*Heslop and Dillon*, 2007] to unmix down-core variations in coercivity components for 86 IRM samples (Figure 5a) from the 0–34 m depth range in core MD01-2421. Details of this method are described by *Heslop* [2015]. Our analysis indicates that a good fit (i.e., a high r^2 value) [*Heslop and Dillon*, 2007] is achieved with two IRM coercivity components (soft and hard; Figures 5b and 5c). The modeled hard component has a slightly smaller DP (blue line in Figure 5c) compared to the softer component, which is consistent with IRM analysis of individual samples (Figure 4f). Again, large DP values were fitted for both EMs. We plot down-core variations of the modeled EMs (both relative proportion and absolute concentrations; Figure 5i), along with hysteresis parameters (Figures 5d–5g) and elemental S variations (Figure 5h). The high-magnetization intervals generally contain more of the soft than the hard component (Fig. 5i). This is consistent with hysteresis measurements, which indicate that the high-magnetization intervals contain more low coercivity magnetic minerals.

4.4. SEM and TEM Observations

Magnetic extracts for sample "MD01-2421-7-110" (from a depth of 10.06 m; indicated by a blue star in Figure 2) were analyzed with SEM (Figures 6a–6f) and TEM (Figures 6h and 6i). This sample has intermediate hysteresis parameter values ($B_c = 26.3$ mT; $B_{cr} = 63.0$ mT; $M_{rs}/M_s = 0.289$; $B_{cr}/B_c = 2.40$) with respect to the two end-members. SEM observations indicate abundant Fe-Ti oxides with a wide range of sizes and morphologies. These include well-preserved large titanomagnetite crystals (>10 μm; Figure 6a), titanohematite ($Fe_{2-x}Ti_xO_3$) lamellae (Figures 6b–6d), silicate-hosted titanomagnetite dendritic textures (arrows in Figure 6e), and isolated titanomagnetite nanoparticles within silicates (arrows in Figure 6f). Euhedral pyrite crystals ($\sim$4 μm) are also observed (arrows in Figure 6b). Titanomagnetites have much higher Fe-Ti ratios compared to those of paramagnetic titanohematite (including ilmenite ($FeTiO_3$)). These characteristics enable discrimination of titanomagnetite from titanohematite in sediments [*Franke et al*., 2007]. EDS results are presented in Figure 6g, where Fe-Ti oxides have two distinct groups of Fe-Ti ratios: the large Fe-Ti oxide grain (Figure 6a) and nanoparticle inclusions (Figures 6e and 6f) have much higher Fe-Ti ratios compared to the Fe-Ti oxide lamellae structures (Figures 6b–6d), which correspond to titanomagnetites (Figures 6a, 6e, and 6f) and titanohematites (Figures 6b–6d), respectively.

TEM observations (Figures 6h and 6i) of the same sample used for SEM analysis reveal abundant large detrital magnetic grains. Most of these grains are too thick for electron transmission and appear dark under TEM. We selected thinner edge areas from large grains for TEM analysis. An example of such an analysis is shown in Figure 6h (NB: the darker areas are from the thicker part of the grain). Abundant magnetic nanoparticles, some of which are several tens of nanometers across (arrows in Figure 6h), were observed within a host silicate mineral, as have been observed in igneous rocks of various types [e.g., *Feinberg et al*., 2005; *Tarduno et al*., 2006]. Some of these nanoparticles are elongated and have a generally uniform orientation within host grains. We also observed fine-grained magnetite particles (Figure 6i) that do not occur within host minerals. They also have sharp crystal morphologies, such as octahedral, prismatic, and bullet shapes, that are typical of fine-grained biogenic magnetite that were originally produced by magnetotactic bacteria [e.g., *Roberts et al*., 2012]. Biogenic magnetite crystals within this studied sample are much less abundant in

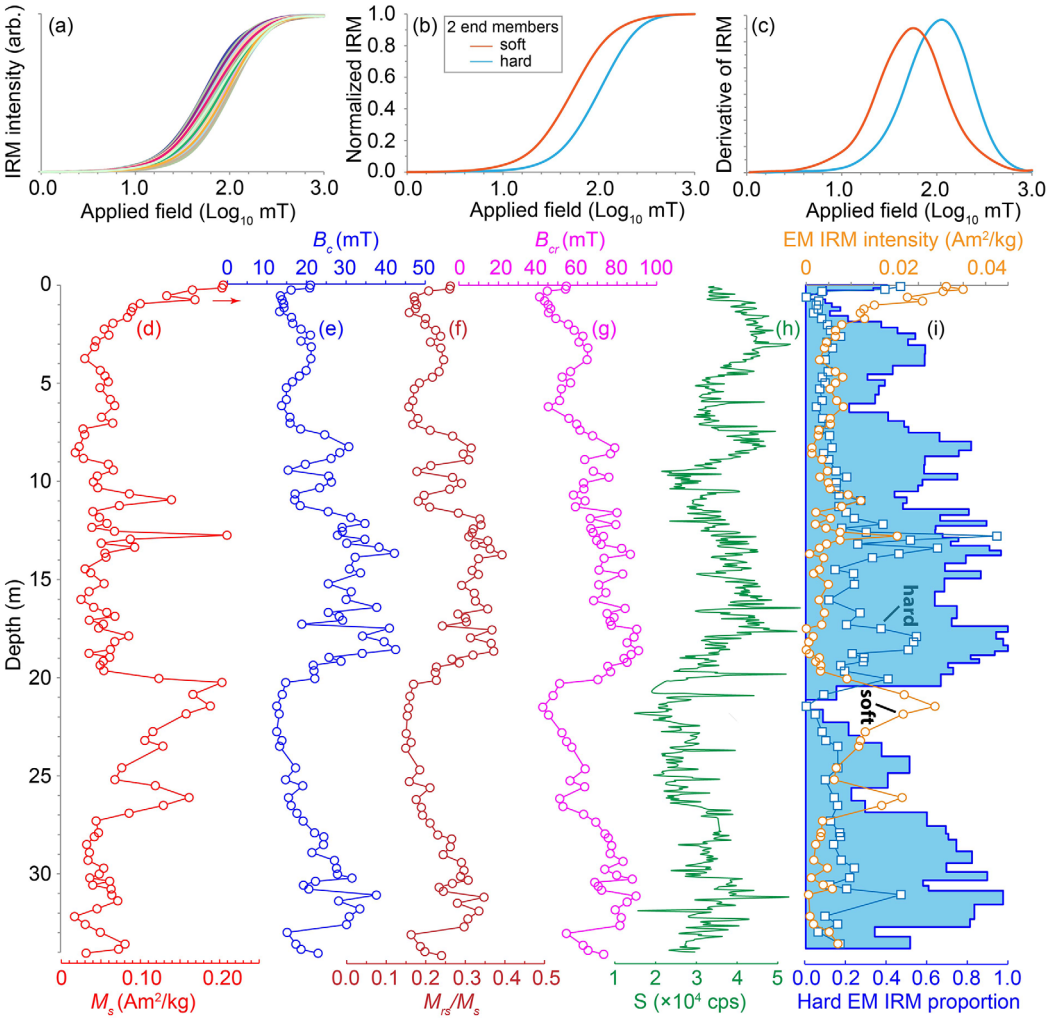

Figure 5. End-member modeling of IRM acquisition curves measured for discrete samples from core MD01-2421. (a) Measured IRM acquisition curves for 86 samples from the 0–34 m depth interval. Data are normalized to the maximum IRM value. (b) IRM curves and (c) derivative of IRM curves for a two-end-member model calculated from all of the experimental IRM curves in Figure 5a. (d-g) Hysteresis parameters and (h) S content, which are plotted along with (i) down-core variations for the two IRM end-members. The filled region (blue) represents the proportion of the hard IRM EM component through the core. The remaining proportion is, therefore, representative of the soft IRM EM component.

TEM observations compared to magnetofossil-rich sediments [e.g., *Chang et al.*, 2012; *Heslop et al.*, 2013; *Roberts et al.*, 2013].

5. Discussion

5.1. Magnetic Mineralogy and Origin of Down-Core Magnetic Patterns: Variable Diagenetic Alteration and Preservation of Magnetic Mineral Inclusions

Our magnetic and electron microscopic analyses consistently indicate that the dominant magnetic minerals throughout the studied core are inorganic magnetite and titanomagnetite. These analyses also preclude the presence of magnetically measurable concentrations of other common sedimentary magnetic minerals (i.e., detectable rock magnetic properties of these magnetic minerals). Greigite (Fe_3S_4) was not detected in either electron microscopic analyses or through its characteristic magnetic properties. For example, thermomagnetic curves for greigite often decrease significantly below ~400°C due to thermal decomposition [e.g., *Snowball and Thompson*, 1988; *Chang et al.*, 2008; *Roberts et al.*, 2011]. FORC diagrams for the studied samples indicate moderate magnetostatic interactions and broad coercivity distributions, which are distinct from those for diagenetic greigite [*Roberts et al.*, 2011]. Fitted DP values for the studied samples are ~0.3

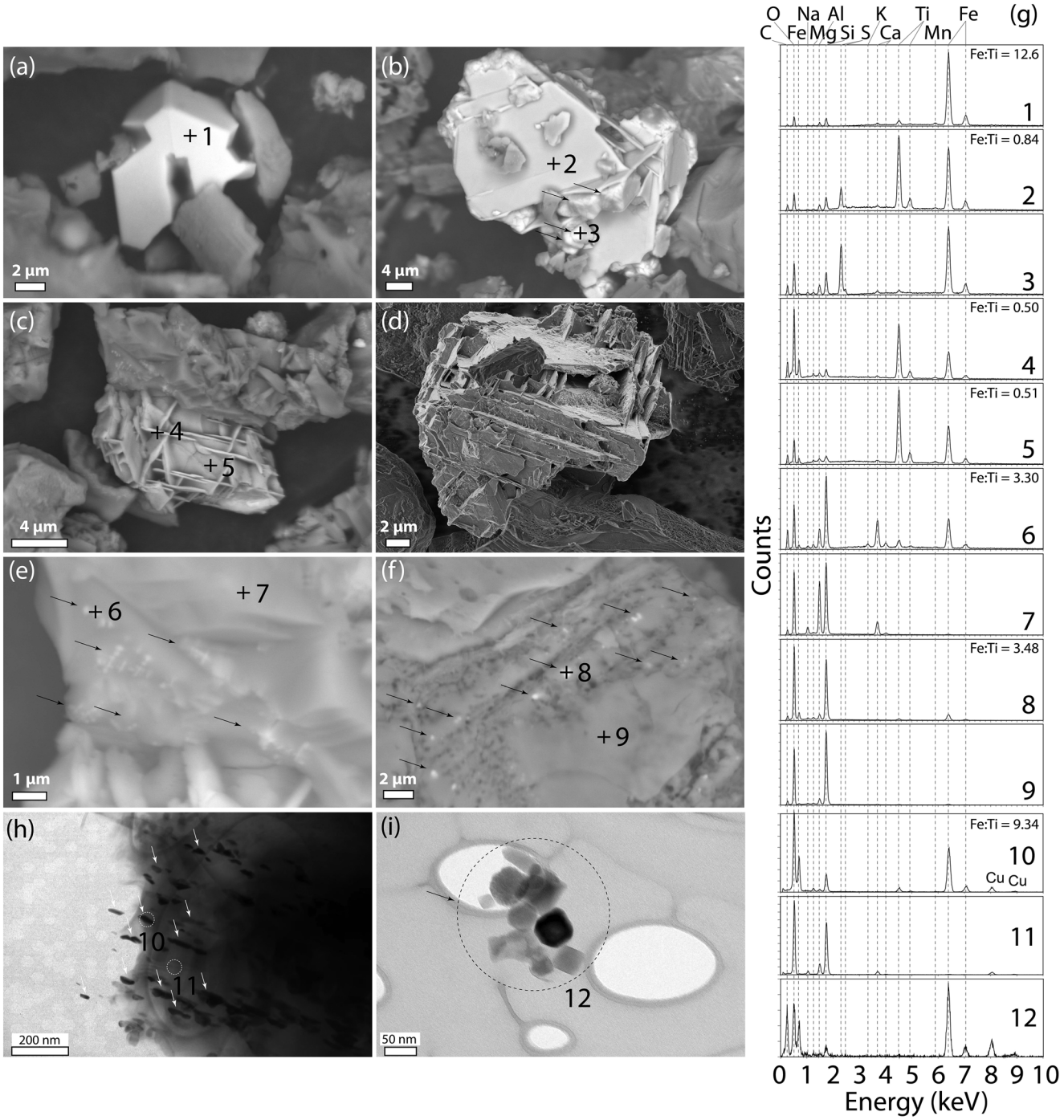

Figure 6. (a-f) SEM and (h, i) bright-field TEM images of magnetic extracts from sample "MD01-2421-7-110" (from a depth of 10.06 m) and (g) selected energy-dispersive spectra for numbered spots indicated within the SEM and TEM images. (a) A well-preserved Ti-poor titanomagnetite grain. (b–d) Titanohematite lamellae structures. Euhedral pyrite crystals are also detected (arrows in Figure 6b). (e) Titanomagnetite dendritic textures (arrows) embedded in a silicate host grain. (f) Isolated titanomagnetite nanoparticles (arrows) within a silicate particle. (d) A high-resolution SEM image acquired using the Inlens detector at 2 kV. All other SEM images are backscattered electron images acquired at 15 kV. Numbered crosses indicate EDS analysis spots, as presented in Figure 6g. C peaks in the EDS spectra originate from the carbon coatings on the samples. (h) TEM image of titanomagnetite nanoparticle intergrowths (arrows) within a silicate host mineral. The image was taken on the edge of the silicate grain. (i) Probable biogenic magnetite nanoparticles (arrows). The lower three TEM based EDS spectra in Figure 6g were collected from circled areas in Figures 6h and 6i: spectrum (10) titanomagnetite nanoparticle inclusion in Figure 6h, spectrum (11) host silicate mineral in Figure 6h, and spectrum (12) biogenic magnetite nanoparticles in Figure 6i. Cu peaks originate from the TEM grid. C is from the carbon film on the TEM grid. The EDS spectrum (10) also contains signals from the silicate host mineral in which the titanomagnetite is embedded.

(Figure 4f), which is significantly larger than for diagenetic greigite [*Chang et al.*, 2014b]. Titanomaghemite is often associated with low-temperature oxidation of titanomagnetite of volcanic origin and may be present [e.g., *Doubrovine and Tarduno*, 2006], but its presence within the studied samples should not affect our

main interpretations. TEM observations reveal small amounts of biogenic magnetite crystals, but most studied samples lack detectable magnetic signatures for biogenic magnetite. For example, FORC diagrams do not have a characteristic central-ridge feature [*Egli et al*., 2010; *Roberts et al*., 2012; *Chang et al*., 2014a]. The major IRM components have large DP values (mostly between 0.3 and 0.4), unlike the typical low values for the narrow grain size distributions associated with biogenic magnetite crystals [*Kruiver and Passier*, 2001]. Clearly, some biogenic magnetite crystals have survived reductive diagenesis (Figure 6i). The fact that some biogenic crystals were detected by TEM but not by magnetic analyses is likely due to their different sensitivity for detecting biogenic magnetite [e.g., *Chang et al*., 2014a]. For example, magnetic detection of biogenic magnetite requires that it must be present in large enough concentrations with respect to coarse-grained detrital magnetic particles. In contrast, TEM sample preparation can enable preferential extraction of biogenic magnetite crystals that can be detected in much lower concentrations [e.g., *Chang et al*., 2012, 2014a]. The large DP values for the studied samples indicate a broad grain size distribution, and are indicative of a detrital origin of constituent magnetic minerals sourced from different regions [*Egli*, 2004]. The dominant magnetite and titanomagnetite (with variable Ti content) within the studied samples have a terrigenous provenance, likely from erosion of igneous rocks from Japan.

Our analysis indicates that magnetic and geochemical properties are broadly correlated throughout the core: more strongly magnetized intervals (i.e., high M_s) contain more low coercivity magnetic minerals mostly in the PSD/MD size range and have lower S (i.e., pyrite), and *vice versa* (Figure 2). Samples from more weakly magnetized intervals contain a higher titanomagnetite concentration with more SD-like properties (Figure 2, S3). This interpretation of down-core patterns is further supported by IRM end-member modeling (Figure 5). The observed correlation between magnetic and geochemical parameters suggests a cyclic variation of sulfidic diagenesis intensity (indicated by S variations) due to covarying OC supply (indicated by TOC). Cycles of nonsteady state diagenetic variations, which control the magnetic properties of such sediments through time-varying movement of diagenetic fronts, are well documented for sediments with time-varying OC burial [e.g., *Tarduno*, 1994; *Larrasoaña et al*., 2003; *Roberts*, 2015]. Below, we explore the processes that are interpreted to have given rise to the magnetic and geochemical property variations in core MD01-2421.

Down-core magnetic mineral coarsening in surface sediments is often reported because reductive diagenesis tends to first dissolve small ferric phases due to their reactivity and larger surface area to volume ratio [e.g., *Karlin and Levi*, 1983; *Garming et al*., 2005; *Rowan et al*., 2009; *Roberts*, 2015; *Chang et al*., 2016]. *Karlin and Levi* [1985] observed a down-core fining of magnetic minerals in hemipelagic sediments, just below the uppermost surface sediments where the initially rapid down-core coarsening occurs. This fining signature was also documented by *Tarduno* [1995] within sediments from the western equatorial Pacific Ocean. Our data indicate that a similar diagenetically induced fining mechanism occurs in core MD01-2421, and that such a process must have acted repeatedly. In a nonsteady state diagenetic scenario, varying strengths of diagenesis would have led to variable modification of the original detrital magnetic mineral assemblages and hence to varying magnetite and titanomagnetite mixtures: less severe sulfidic conditions favored preservation of both types of minerals, while more severe sulfidic conditions led to more magnetite being dissolved with preferential preservation of Fe-Ti oxides. Titanomagnetite is more stable against dissolution [*Karlin*, 1990b; *Emiroğlu et al*., 2004; *Garming et al*., 2005] because the reactivity of Fe-Ti oxides to sulfide is lower than for stoichiometric magnetite [*Canfield et al*., 1992; *Poulton et al*., 2004; *Roberts*, 2015]. Increasing titanium content can stabilize titanomagnetite grains against sulfidic dissolution because Ti^{4+} substitution reduces the concentration of the acting electron acceptor Fe^{3+}. A more important factor is the protection of titanomagnetite nanoparticles against sulfidic diagenesis by host silicate grains (Figures 3 and 6e–6h) because silicates are largely unreactive to sulfide [*Canfield et al*., 1992; *Poulton et al*., 2004; *Roberts*, 2015].

The overall diagenetic process discussed above is illustrated schematically in Figure 7, where we highlight the role of magnetic mineral inclusions in recording diagenetic and environmental magnetic signals. Such diagenetically filtered records, which are modulated through environment variability, may be common in marine environments, for example, in sediments from the Argentine continental slope [*Riedinger et al*., 2005; *Garming et al*., 2005], Niger deep-sea fan [*Dillon and Bleil*, 2006], Gulf of California [*Karlin and Levi*, 1985], and East China Sea [*Zheng et al*., 2010]. Such sedimentary diagenetic magnetic mineral alteration will have important implications for paleoenvironmental and paleomagnetic studies. For example, the sediments would not pass the standard criteria for constant input/preservation for studying sedimentary

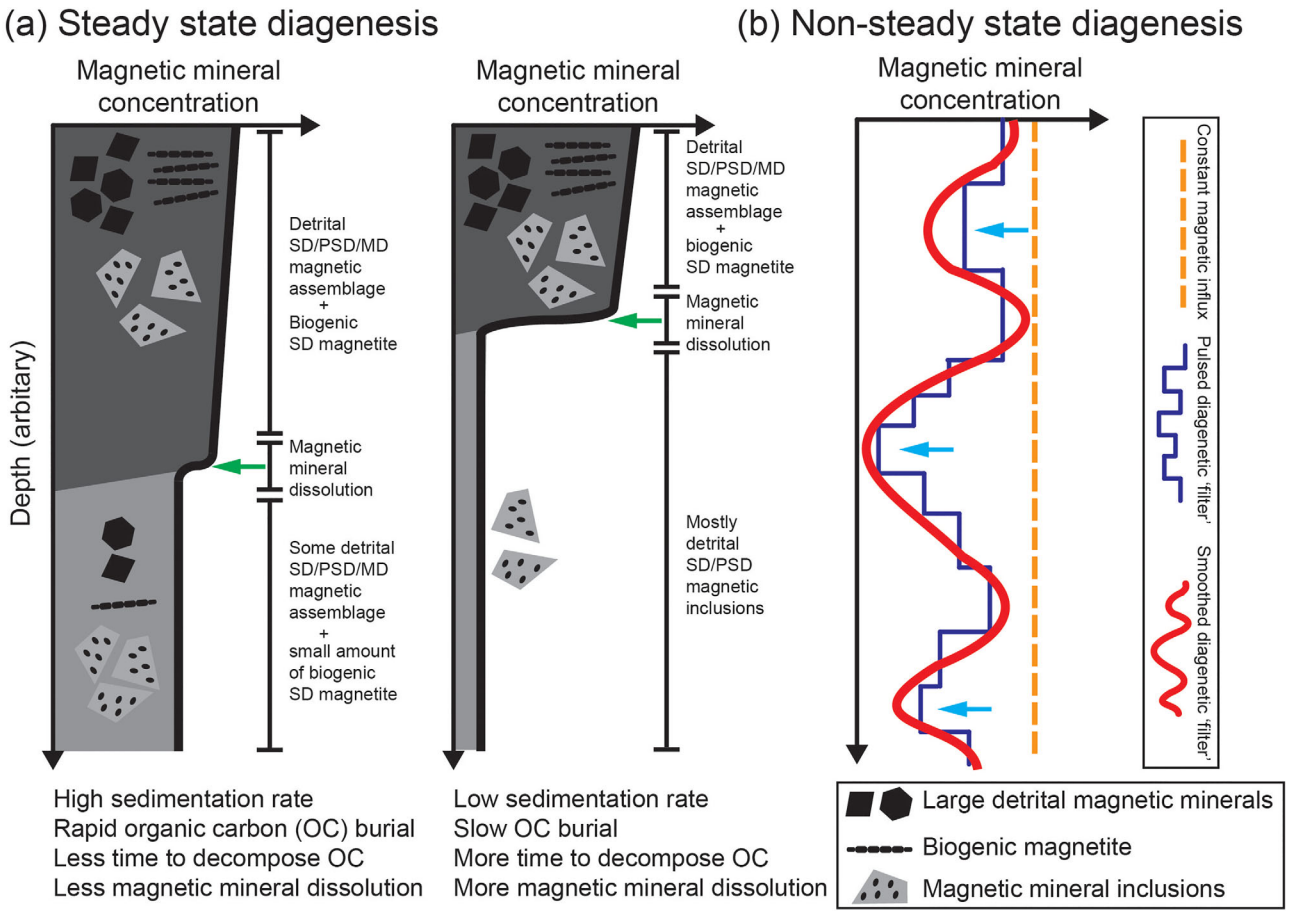

Figure 7. Schematic illustration of magnetic mineral diagenetic processes that control down-core magnetic and geochemical patterns at the studied site. (a) Two scenarios of steady state diagenesis. In Figure 7a, high sedimentation rates and OC inputs give rise to rapid OC burial so that a significant magnetic mineral assemblage can be preserved. In contrast, lower sedimentation rate and high OC inputs result in stronger magnetic mineral diagenesis. Most of the surviving magnetic minerals occur as inclusions within larger silicate particles due to the protection of silicate host minerals. Green arrows in Figure 7a mark the position of the dissolution front. (b) Schematic illustration of nonsteady state diagenesis with shifting sedimentation rate and OC burial. Blue arrows in Figure 7b mark stratigraphic intervals with enhanced expression of magnetic signatures from magnetic mineral inclusions.

relative paleointensity [*Tauxe*, 1993], or for tracing sediment provenance because of significant postdepositional magnetic mineral alteration.

5.2. A Lagged Marine Diagenetic Record of Asian Monsoon Variations

Diagenesis is a postdepositional process with reaction fronts that can occur several meters below the sediment-water interface [e.g., *Schulz and Zabel*, 2006; *Roberts*, 2015]. Therefore, an offset between the forcing and the resulting diagenetic signature is expected (i.e., through variable influx, burial, and degradation of OC) due to diffusion of pore fluids at dissolution fronts that is affected by degradation of the overlying OC. Identification of the active sulfidic dissolution front that occurs within the uppermost part of a core site [e.g., *Karlin*, 1990a,b; *Riedinger et al.*, 2005; *Rowan et al.*, 2009; *Roberts*, 2015; *Chang et al.*, 2016] provides a means to estimate the diagenetic lag with respect to the forcing. Two distinct zones are observed within the upper meter of core MD01-2421 (Figure 8). In zone 1, there is a marked decrease in magnetic mineral concentration (Figures 8b–8d), as indicated by ARM (Figure 8c) and M_s (Figure 8d). ARM intensity is sensitive to SD magnetic particles [*Dunlop and Özdemir*, 1997]. The sharp ARM decline in zone 1 (Figure 8c) is probably associated with fine-grained SD particle dissolution [*Rowan et al.*, 2009], including biogenic magnetite [*Chang et al.*, 2016]. Zone 2 is characterized by a further magnetic mineral concentration decrease (Figures 8b and 8d), and a coercivity increase (Figure 8e). This pattern is interpreted to correspond to further dissolution of coarse detrital magnetic particles [*Rowan et al.*, 2009]. Within zones 1 and 2, diagenetic pyrite continues to grow (Figure 8f). We estimate a ~3.5 kyr penetration of the present-day sulfidic dissolution front into deeper sediments (Figure 8), although such estimates can be affected by second-order factors such as

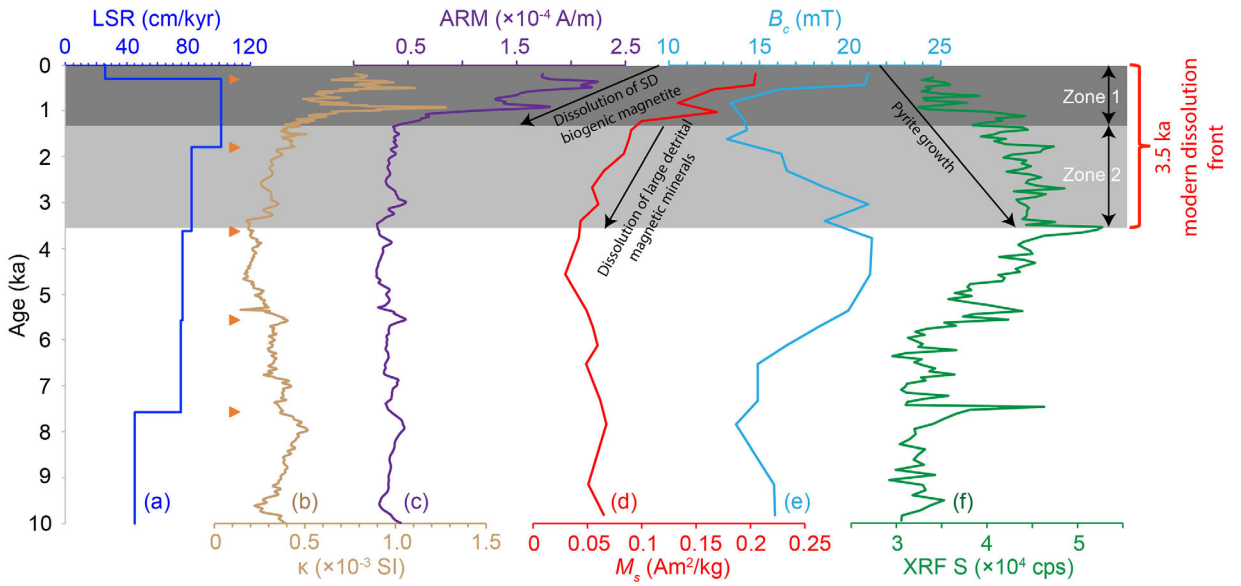

Figure 8. Magnetic and geochemical parameters for the uppermost interval of core MD01-2421. (a) Linear sedimentation rate (LSR) with age tie points (orange triangles), (b) κ, (c) ARM, (d) M_s, (e) B_c, and (f) elemental (XRF) S content. Zones 1 and 2 contain evidence of progressive dissolution of fine-grained biogenic magnetite and coarse-grained detrital magnetic minerals, respectively. Within zones 1 and 2, diagenetic pyrite continues to grow postdepositionally. A ~3.5 kyr age offset is estimated for the position of the modern dissolution front. Profiles are shown on an age scale to better demonstrate the age offset, though diagenesis is a depth-dependent process.

sedimentation rate changes, which can be affected by other factors such as tectonic changes in sediment source regions.

Based on the above, we propose a correlation (Figure 9) of the core MD01-2421 diagenetic record (represented by elemental S) to the well-dated Asian monsoon stalagmite record from Hulu Cave (32°30′N; 119°10′E), China [*Wang et al*., 2001]. Hulu Cave, which is close to the studied core site (Figure 1), provides an iconic and representative record of Asian monsoon variations. Two main assumptions have been made in proposing this correlation (Figure 9). First, we correlate diagenetic maxima (i.e., pyrite and coercivity maxima) to strong Asian monsoon intensities that correspond to interstadial climate events in the northern North Atlantic region. Pyrite minima (weaker diagenesis) are, thus, linked to major colder Asian monsoon periods and Heinrich events (Figure 9; horizontal bars). Monsoon-induced OC variations have been well documented elsewhere, including in sediment cores from the Arabian Sea, which correlate well to Greenland ice core records, i.e., low TOC values are associated with intervals of high-latitude cooling [*Schulz et al*., 1998]. Changes in Asian monsoon intensity also appear to be the dominant driving force for OC supply to the studied site. Second, age offsets of a few kyr due to time-varying downward diffusion of sulfidic dissolution fronts are apparent. There is a general similarity between our marine diagenetic and the Hulu Cave records, by considering lags between times of strong monsoon activity and S anomalies in core MD01-2421 (Figure 9). We assume that changes in magnetic and geochemical proxies essentially reflect activity at the HS^- front and that all other changes that affect magnetic mineral assemblages (i.e., different sources of lithogenic sediment sources, reactions at the overlying Fe-redox boundary, the presence of upward migrating diagenetic fronts, and tectonic events) appear to be second-order factors and have been largely overprinted by subsequent sulfidic diagenesis. The assumption of an overriding influence of reductive diagenesis is reasonable considering that the studied core is from a marine environment with a high OC content. It is difficult to assess the effects of other sedimentary processes based on currently available datasets. Nevertheless, our correlation is supported by the well-established chronology of the studied core, which is based on a combination of benthic foraminiferal $\delta^{18}O$, ^{14}C ages of 12 mixed planktonic foraminifera samples, and one ash layer (Figure 9a; *Oba et al*. [2006]). The late Pleistocene sedimentation rate was much higher than in the Holocene (Figure 9a). Such a shift is consistent with greater OC preservation during the Holocene (Figure 2f). In contrast, lower sedimentation rates in the late Pleistocene resulted in decreased OC perseveration, which produced a more pronounced signature from relict magnetic mineral inclusions within silicate particles than in the Holocene.

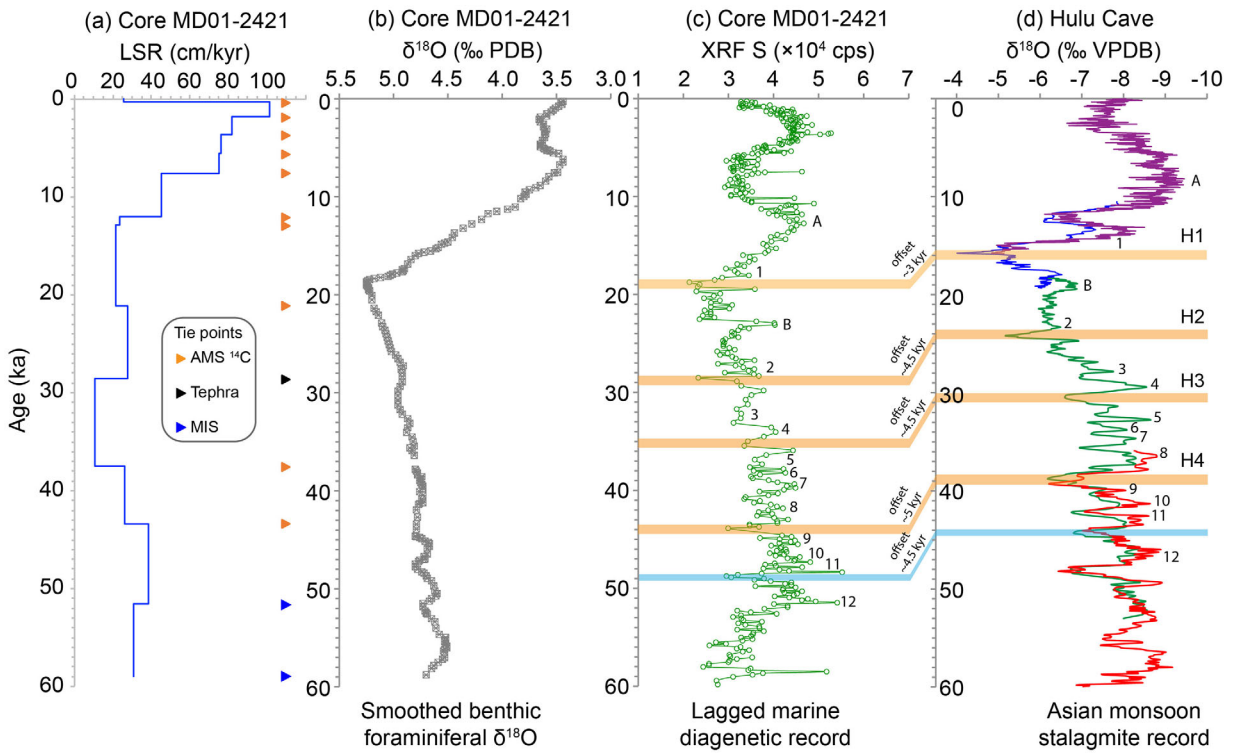

Figure 9. (a) LSR and age tie points (triangles) for core MD01-2421, (b) δ^{18}O record from benthic foraminifera [*Oba et al.*, 2006] and (c) diagenetic record (elemental (XRF) S content) for core MD01-2421 for the last 60 ka, and a proposed correlation between this lagged diagenetic record and (d) the Hulu Cave stalagmite record of Asian monsoon variations [*Wang et al.*, 2001]. Yellow bars indicate the positions of Heinrich events (H1–H4). Numbers and yellow bars in Figure 9d are the same as in *Wang et al.* [2001]. A–B in Figures 9c and 9d and the numbers indicate possible correlations. Please note the age offsets between (Figure 9d) the forcing and (Figure 9c) the diagenetic response. The 3–5 kyr lags in the diagenetic record with respect to the Asian monsoon record are consistent with the ~3.5 ka age estimate for the position of the modern dissolution front. The δ^{18}O record in Figure 9b is a smoothed three-point average of the measured data [*Oba et al.*, 2006].

Monsoon-induced oceanographic changes could have driven higher OC preservation at the seafloor through two mechanisms: by control of OC export to the seafloor or by enhancing OC burial in association with greater ocean stratification, which reduces bottom water ventilation and enhances preservation of buried OC. We cannot discriminate between these possibilities with available data. Regardless, enhanced OC burial, likely driven by changes in Asian monsoon intensities, promoted variable sulfidic diagenesis that resulted in time-varying magnetic mineral dissolution and pyrite formation. Connections between the Asian monsoon and North Atlantic climate have been well documented [e.g., *Porter and An*, 1995; *Wang et al.*, 2001; *Rohling et al.*, 2003, 2009; *Sun et al.*, 2012; *Grant et al.*, 2014]. This large-scale climatic teleconnection appears to be reflected in our diagenetic record.

6. Conclusions

Analysis of a deep-sea sediment core from offshore of Japan indicates correlations among magnetic parameters and geochemical variations, where magnetization minima correlate to coercivity and elemental S maxima, and *vice versa*. Magnetic and electron microscope analyses indicate that relict titanomagnetite preserved as inclusions within larger silicate particles play an important role in strongly diagenetically altered sediment intervals. Such magnetic and geochemical patterns appear to be associated with selective and variable dissolution/preservation of magnetic minerals under continuously shifting diagenetic conditions, associated with variable organic carbon burial and decomposition. This study demonstrates the importance of magnetic mineral inclusions for recording environmental magnetic signals. We correlate millennial-scale variations in magnetic mineral diagenesis with changes in overlying organic carbon burial, which was likely driven by Asian monsoon fluctuations. Our magnetic and geochemical analysis enables identification of offsets between the positions of fossil diagenetic fronts and climatically induced variations in organic carbon burial. We suggest that episodes of intense monsoon

activity and attendant sediment magnetic mineral diagenesis also correlate with Heinrich events, which supports other documented indications of teleconnections between North Atlantic and Asian climate forcing.

Acknowledgments
We thank Tadamichi Oba of Hokkaido University, Japan, for providing u-channel samples and data. The data in this paper can be obtained by contacting the corresponding author (liao.chang@pku.edu.cn). The data is available at the RMAG portal (rock magnetic database) of the Magnetics Information Consortium (http://earthref.org/MAGIC/). We thank staff at the Centre for Advanced Marine Core Research at Kochi University and JAMSTEC for their assistance to this project. John Tarduno and two anonymous reviewers provided useful suggestions that improved the manuscript significantly. We thank Editor Joshua Feinberg for his efficient editorial handling. This study was supported by the Japan Society for the Promotion of Science "Invitational Programs for Advanced Japanese Research Institutes." Additional funding from the Netherlands Organization for Scientific Research, the Australian Research Council (grants DP120103952 and DP140104544), the "1000 Talents Plan" program of China, and the National Natural Science Foundation of China (grant 41574060) enabled completion of this work.

References

Abrajevitch, A., and K. Kodama (2011), Diagenetic sensitivity of paleoenvironmental proxies: A rock magnetic study of Australian continental margin sediments, *Geochem. Geophys. Geosyst.*, *12*, Q05Z24, doi:10.1029/2010GC003481.

Blanchet, C. L., N. Thouveny, and L. Vidal (2009), Formation and preservation of greigite (Fe_3S_4) in sediments from the Santa Barbara Basin: Implications for paleoenvironmental changes during the past 35 ka, *Paleoceanography*, *24*, PA2224, doi:10.1029/2008PA001719.

Bouilloux, A., J.-P. Valet, F. Bassinot, J.-L. Joron, M.-M. Blanc-Valleron, E. Moreno, F. Dewilde, M. Kars, and F. Lagroix (2013), Diagenetic modulation of the magnetic properties in sediments from the Northern Indian Ocean, *Geochem. Geophys. Geosyst.*, *14*, 3779–3800, doi:10.1002/ggge.20234.

Canfield, D. E., R. Raiswell, and S. H. Bottrell (1992), The reactivity of sedimentary iron minerals toward sulfide, *Am. J. Sci.*, *292*, 659–683.

Chang, L., A. P. Roberts, Y. Tang, B. D. Rainford, A. R. Muxworthy, and Q. Chen (2008), Fundamental magnetic parameters from pure synthetic greigite (Fe_3S_4), *J. Geophys. Res.*, *113*, B06104, doi:10.1029/2007JB005502.

Chang, L., A. P. Roberts, W. Williams, J. D. Fitz Gerald, J. C. Larrasoaña, L. Jovane, and A. R. Muxworthy (2012), Giant magnetofossils and hyperthermal events, *Earth Planet. Sci. Lett.*, *351–352*, 258–269, doi:10.1016/j.epsl.2012.07.031.

Chang, L., A. P. Roberts, M. Winklhofer, D. Heslop, M. J. Dekkers, W. Krijgsman, J. D. Fitz Gerald, and P. Smith (2014a), Magnetic detection and characterization of biogenic magnetic minerals: A comparison of ferromagnetic resonance and first-order reversal curve diagrams, *J. Geophys. Res.*, *119*, 6136–6158, doi:10.1002/2014JB011213.

Chang, L., I. Vasiliev, C. van Baak, W. Krijgsman, M. J. Dekkers, A. P. Roberts, J. D. Fitz Gerald, A. van Hoesel, and M. Winklhofer (2014b), Identification and environmental interpretation of diagenetic and biogenic greigite in sediments: A lesson from the Messinian Black Sea, *Geochem. Geophys. Geosyst.*, *15*, 3612–3627, doi:10.1002/2014GC005411.

Chang, L., D. Heslop, A. P. Roberts, D. Rey, and K. J. Mohamed (2016), Discrimination of biogenic and detrital magnetite through a double Verwey transition temperature, *J. Geophys. Res. Solid Earth*, *121*, 3–14, doi:10.1002/2015JB012485.

Day, R., M. Fuller, and V. A. Schmidt (1977), Hysteresis properties of titanomagnetites: Grain size and compositional dependence, *Phys. Earth Planet. Inter.*, *13*, 260–267.

Dillon, M., and U. Bleil (2006), Rock magnetic signatures in diagenetically altered sediments from the Niger deep-sea fan, *J. Geophys. Res.*, *111*, B03105, doi:10.1029/2004JB003540.

Doubrovine, P. V., and J. A. Tarduno (2006), Alteration and self-reversal in oceanic basalts, *J. Geophys. Res.*, *111*, B12S30, doi:10.1029/2006JB004468.

Dunlop, D. J., and Ö. Özdemir (1997), *Rock Magnetism: Fundamentals and Frontiers*, 573 pp., Cambridge Univ. Press, Cambridge, U. K.

Egli, R. (2004), Characterization of individual rock magnetic components by analysis of remanence curves: 1. Unmixing natural sediments, *Stud. Geophys. Geod.*, *48*, 391–446, doi:10.1023/B:SGEG.0000020839.45304.6d.

Egli, R., A. P. Chen, M. Winklhofer, K. P. Kodama, and C.-S. Horng (2010), Detection of noninteracting single domain particles using first-order reversal curve diagrams, *Geochem. Geophys. Geosyst.*, *11*, Q01Z11, doi:10.1029/2009GC002916.

Emiroğlu, S., D. Rey, and N. Petersen (2004), Magnetic properties of sediments in the Ría de Arousa (Spain): Dissolution of iron oxides and formation of iron sulphides, *Phys. Chem. Earth*, *29*, 947–959.

Feinberg, J. M., G. R. Scott, P. R. Renne, and H. R. Wenk (2005), Exsolved magnetite inclusions in silicates: Features determining their remanence behavior, *Geology*, *33*, 513–516.

Franke, C., G. M. Pennock, M. R. Drury, R. Engelmann, D. Lattard, J. F. L. Garming, T. von Dobeneck, and M. J. Dekkers (2007), Identification of magnetic Fe-Ti oxides in marine sediments by electron backscatter diffraction in scanning electron microscopy, *Geophys. J. Int.*, *170*, 545–555.

Garming, J. F. L., U. Bleil, and N. Riedinger (2005), Alteration of magnetic mineralogy at the sulphate-methane transition: Analysis of sediments from the Argentine continental slope, *Phys. Earth Planet. Inter.*, *151*, 290–308.

Grant, K. M., et al. (2014), Sea-level variability over five glacial cycles, *Nat. Commun.*, *5*, 5076, doi:10.1038/ncomms6076.

Heslop, D. (2015), Numerical strategies for magnetic mineral unmixing, *Earth Sci. Rev.*, *150*, 256–284.

Heslop, D., and M. Dillon (2007), Unmixing magnetic remanence curves without *a priori* knowledge, *Geophys. J. Int.*, *170*, 556–566.

Heslop, D., and A. P. Roberts (2012), Estimation of significance levels and confidence intervals for first-order reversal curve distributions, *Geochem. Geophys. Geosyst.*, *13*, Q12Z40, doi:10.1029/2012GC004115.

Heslop, D., A. P. Roberts, L. Chang, M. Davies, A. Abrajevitch, and P. De Deckker (2013), Quantifying magnetite magnetofossil contributions to sedimentary magnetizations, *Earth Planet. Sci. Lett.*, *382*, 58–65.

Itambi, A. C., T. von Dobeneck, M. J. Dekkers, and T. Frederichs (2010), Magnetic mineral inventory of equatorial Atlantic Ocean marine sediments off Senegal–glacial and interglacial contrast, *Geophys. J. Int.*, *183*, 163–177.

Karlin, R. (1990a), Magnetite diagenesis in marine sediments from the Oregon continental margin, *J. Geophys. Res.*, *95*, 4405–4419, doi:10.1029/JB095iB04p04405.

Karlin, R. (1990b), Magnetic mineral diagenesis in suboxic sediments at Bettis site W-N, NE Pacific Ocean, *J. Geophys. Res.*, *95*, 4421–4436, doi:10.1029/JB095iB04p04421.

Karlin, R., and S. Levi (1983), Diagenesis of magnetic minerals in recent haemipelagic sediments, *Nature*, *303*, 327–330.

Karlin, R., and S. Levi (1985), Geochemical and sedimentological control of the magnetic properties of hemipelagic sediments, *J. Geophys. Res.*, *90*, 10,373–10,392.

Kawamura, N., N. Ishikawa, and M. Torii (2012), Diagenetic alteration of magnetic minerals in Labrador Sea sediments (IODP Sites U1305, U1306, and U1307), *Geochem. Geophys. Geosyst.*, *13*, Q08013, doi:10.1029/2012GC004213.

Kruiver, P. P., and H. F. Passier (2001), Coercivity analysis of magnetic phases in sapropel S1 related to variations in redox conditions, including an investigation of the S ratio, *Geochem. Geophys. Geosyst.*, *2*, 1063, doi:10.1029/2001GC000181.

Kruiver, P. P., M. J. Dekkers, and D. Heslop (2001), Quantification of magnetic coercivity components by the analysis of acquisition curves of isothermal remanent magnetization, *Earth Planet. Sci. Lett.*, *189*, 269–276, doi:10.1016/S0012-821X(01)00367-3.

Larrasoaña, J. C., A. P. Roberts, J. S. Stoner, C. Richter, and R. Wehausen (2003), A new proxy for bottom-water ventilation in the eastern Mediterranean based on diagenetically controlled magnetic properties of sapropel-bearing sediments, *Palaeogeogr. Palaeoclimatol. Palaeoecol.*, *190*, 221–242.

Liu, Q., A. P. Roberts, J. C. Larrasoaña, S. K. Banerjee, Y. Guyodo, L. Tauxe, and F. Oldfield (2012), Environmental magnetism: Principles and applications, *Rev. Geophys.*, *50*, RG4002, doi:10.1029/2012RG000393.
Mullender, T. A. T., A. J. van Velzen, and M. J. Dekkers (1993), Continuous drift correction and separate identification of ferrimagnetic and paramagnetic contributions in thermomagnetic runs, *Geophys. J. Int.*, *114*, 663–672.
Muxworthy, A. R., and D. J. Dunlop (2002), First-order reversal curve (FORC) diagrams for pseudo-single-domain magnetites at high temperature, *Earth Planet. Sci. Lett.*, *203*, 369–382.
Oba, T., T. Irino, M. Yamamoto, M. Murayama, A. Takamura, and K. Aoki (2006), Paleoceanographic change off central Japan since the last 145,000 years based on high-resolution oxygen and carbon isotope records, *Global Planet. Change*, *53*, 5–20, doi:10.1016/j.gloplacha.2006.05.002.
Opdyke, N. D., and J. E. T. Channell (1996), *Magnetic Stratigraphy*, 346 pp., Academic, San Diego, Calif.
Passier, H. F., and M. J. Dekkers (2002), Iron oxide formation in the active oxidation front above sapropel S1 in the eastern Mediterranean Sea as derived from low-temperature magnetism, *Geophys. J. Int.*, *150*, 230–240.
Passier, H. F., G. J. de Lange, and M. J. Dekkers (2001), Magnetic properties and geochemistry of the active oxidation front at the youngest sapropel in the eastern Mediterranean Sea, *Geophys. J. Int.*, *145*, 604–614.
Pike, C. R., A. P. Roberts, and K. L. Verosub (1999), Characterizing interactions in fine magnetic particle systems using first order reversal curves, *J. Appl. Phys.*, *85*, 6660–6667, doi:10.1063/1.370176.
Pike, C. R., A. P. Roberts, M. J. Dekkers, and K. L. Verosub (2001), An investigation of multi-domain hysteresis mechanisms using FORC diagrams, *Phys. Earth Planet. Inter.*, *126*, 11–25.
Porter, S. C., and Z. S. An (1995), Correlation between climate events in the North-Atlantic and China during the last glaciation, *Nature*, *375*, 305–308.
Poulton, S. W., M. D. Krom, and R. Raiswell (2004), A revised scheme for the reactivity of iron (oxyhydr)oxide minerals towards dissolved sulfide, *Geochim. Cosmochim. Acta*, *68*, 3703–3715.
Riedinger, N., K. Pfeifer, S. Kasten, J. F. L. Garming, C. Vogt, and C. Hensen (2005), Diagenetic alteration of magnetic signals by anaerobic oxidation of methane related to a change in sedimentation rate, *Geochim. Cosmochim. Acta*, *69*, 4117–4126.
Roberts, A. P. (2015), Magnetic mineral diagenesis, *Earth Sci. Rev.*, *151*, 1–47.
Roberts, A. P., and G. M. Turner (1993), Diagenetic formation of ferrimagnetic iron sulphide minerals in rapidly deposited marine sediments, New Zealand, *Earth Planet. Sci. Lett.*, *115*, 257–273.
Roberts, A. P., J. S. Stoner, and C. Richter (1999), Diagenetic magnetic enhancement of sapropels from the eastern Mediterranean Sea, *Mar. Geol.*, *153*, 103–116.
Roberts, A. P., C. R. Pike, and K. L. Verosub (2000), First-order reversal curve diagrams: A new tool for characterizing the magnetic properties of natural samples, *J. Geophys. Res.*, *105*, 28,461–28,475, doi:10.1029/2000JB900326.
Roberts, A. P., L. Chang, C. J. Rowan, C.-S. Horng, and F. Florindo (2011), Magnetic properties of sedimentary greigite (Fe_3S_4): An update, *Rev. Geophys.*, *49*, RG1002, doi:10.1029/2010RG000336.
Roberts, A. P., L. Chang, D. Heslop, F. Florindo, and J. C. Larrasoaña (2012), Searching for single domain magnetite in the "pseudo-single-domain" sedimentary haystack: Implications of biogenic magnetite preservation for sediment magnetism and relative paleointensity determinations, *J. Geophys. Res.*, *117*, B08104, doi:10.1029/2012JB009412.
Roberts, A. P., F. Florindo, L. Chang, D. Heslop, L. Jovane, and J. C. Larrasoaña (2013), Magnetic properties of pelagic marine carbonates, *Earth Sci. Rev.*, *127*, 111–139.
Roberts, A. P., D. Heslop, X. Zhao, and C. R. Pike (2014), Understanding fine magnetic particle systems through use of first-order reversal curve diagrams, *Rev. Geophys.*, *52*, 557–602, doi:10.1002/2014RG000462.
Rohling, E. J., P. A. Mayewski, and P. Challenor (2003), On the timing and mechanism of millennial-scale climate variability during the last glacial cycle, *Clim. Dyn.*, *20*, 257–267.
Rohling, E. J., Q. Liu, A. P. Roberts, J. D. Stanford, S. O. Rasmussen, P. L. Langen, and M. Siddall (2009), Controls on the East Asian monsoon during the last glacial cycle, based on comparison between Hulu Cave and polar ice-core records, *Quat. Sci. Rev.*, *28*, 3291–3302.
Rowan, C. J., A. P. Roberts, and T. Broadbent (2009), Reductive diagenesis, magnetite dissolution, greigite growth and paleomagnetic smoothing in marine sediments: A new view, *Earth Planet. Sci. Lett.*, *277*, 223–235.
Sahota, J. T. S., S. G. Robinson, and F. Oldfield (1995), Magnetic measurements used to identify paleoxidation fronts in deep-sea sediments from the Madeira Abyssal Plain, *Geophys. Res. Lett.*, *22*, 1961–1964.
Schulz, H. D., and M. Zabel (2006), *Marine Geochemistry*, Springer, Berlin.
Schulz, H., U. von Rad, and H. Erlenkeuser (1998), Correlation between Arabian Sea and Greenland climate oscillations of the past 110,000 years, *Nature*, *393*, 54–57.
Snowball, I. F., and R. Thompson (1988), The occurrence of greigite in sediments from Loch Lomond, *J. Quat. Sci.*, *3*, 121–125.
Sun, Y., S. C. Clemens, C. Morrill, X. Lin, X. Wang, and Z. An (2012), Influence of Atlantic meridional overturning circulation on the East Asian winter monsoon, *Nat. Geosci.*, *5*, 46–49.
Tarduno, J. A. (1994), Temporal change of magnetic dissolution in the pelagic realm: Gauging paleoproductivity?, *Earth Planet. Sci. Lett.*, *123*, 39–48.
Tarduno, J. A. (1995), Superparamagnetism and reduction diagenesis in pelagic sediments: Enhancement or depletion?, *Geophys. Res. Lett.*, *22*, 1337–1340.
Tarduno, J. A., and S. L. Wilkison (1996), Non-steady state magnetic mineral reduction, chemical lock-in, and delayed remanence acquisition in pelagic sediments, *Earth Planet. Sci. Lett.*, *144*, 315–326.
Tarduno, J. A., R. D. Cottrell, and A. V. Smirnov (2006), The paleomagnetism of single silicate crystals: Recording geomagnetic field strength during mixed polarity intervals, superchrons, and inner core growth, *Rev. Geophys.*, *44*, RG1002, doi:10.1029/2005RG000189.
Tauxe, L. (1993), Sedimentary records of relative paleointensity of the geomagnetic field: Theory and practice, *Rev. Geophys.*, *31*, 319–354.
Thompson, R., and F. Oldfield (1986), *Environmental Magnetism*, 227 pp., Allen and Unwin, London.
Ueshima, T., M. Yamamoto, T. Irino, T. Oba, M. Minagawa, H. Narita, and M. Murayama, (2006), Paleo-productivity record from core MD01-2421, the mid-latitude western North Pacific, during the last 145,000 years, *Global Planet. Change*, *53*, 21–28.
Valet, J.-P., L. Meynadier, and Y. Guyodo (2005), Geomagnetic dipole strength and reversal rate over the past two million years, *Nature*, *435*, 802–805.
van Santvoort, P. J. M., G. J. de Lange, C. G. Langereis, M. J. Dekkers, and M. Paterne (1997), Geochemical and paleomagnetic evidence for the occurrence of "missing" sapropels in eastern Mediterranean sediments, *Paleoceanography*, *12*, 773–786.
Wang, Y. J., H. Cheng, R. L. Edwards, Z. S. An, J. Y. Wu, C.-C. Shen, and J. A. Dorale (2001), A high-resolution absolute-dated late Pleistocene monsoon record from Hulu Cave, China, *Science*, *294*, 2345–2348.

Weeks, R., C. Laj, L. Endignoux, M. Fuller, A. Roberts, R. Manganne, and W. Goree (1993), Improvements in long-core measurement techniques: Applications in palaeomagnetism and palaeoceanography, *Geophys. J. Int.*, *114*, 651–662.

Zheng, Y., C. Kissel, H. B. Zheng, C. Laj, and K. Wang (2010), Sedimentation on the inner shelf of the East China Sea: Magnetic properties, diagenesis and paleoclimate implications, *Mar. Geol.*, *268*, 34–42.